Frontiers of Physics
https://doi.org/10.1007/s11467-020-0952-x
Front. Phys.
15(3), 33602 (2020)

RESEARCH ARTICLE

Bandgap opening in $MoTe_2$ thin flakes induced by surface oxidation

Yuan Gan[1,2], Jiyuan Liang[2], Chang-woo Cho[2], Si Li[3,4], Yanping Guo[2], Xiaoming Ma[2,5], Xuefeng Wu[2], Jinsheng Wen[1], Xu Du[6], Mingquan He[7], Chang Liu[2], Shengyuan A. Yang[4], Kedong Wang[2], Liyuan Zhang[2,†]

[1] *National Laboratory of Solid State Microstructures and Department of Physics, Nanjing University, Nanjing 210093, China*
[2] *Department of Physics, Southern University of Science and Technology, Shenzhen 518055, China*
[3] *School of Physics and Electronics, Hunan Normal University, Changsha 410081, China*
[4] *Research Laboratory for Quantum Materials, Singapore University of Technology and Design, Singapore 487372, Singapore*
[5] *Beijing National Laboratory for Condensed Matter Physics and Institute of Physics, Chinese Academy of Sciences, Beijing 100190, China*
[6] *Department of Physics and Astronomy, Stony Brook University, Stony Brook, NY 11794, USA*
[7] *Chongqing Key Laboratory of Soft Condensed Matter Physics and Smart Materials, College of Physics, Chongqing University, Chongqing 401331, China*
Corresponding author. E-mail: [†] *zhangly@sustech.edu.cn*
Received November 10, 2019; accepted December 27, 2019

Recently, the layered transition metal dichalcogenide 1T′-$MoTe_2$ has generated considerable interest due to their superconducting and non-trivial topological properties. Here, we present a systematic study on 1T′-$MoTe_2$ single-crystal and exfoliated thin-flakes by means of electrical transport, scanning tunnelling microscope (STM) measurements and band structure calculations. For a bulk sample, it exhibits large magneto-resistance (MR) and Shubnikov–de Hass oscillations in ρ_{xx} and a series of Hall plateaus in ρ_{xy} at low temperatures. Meanwhile, the $MoTe_2$ thin films were intensively investigated with thickness dependence. For samples, without encapsulation, an apparent transition from the intrinsic metallic to insulating state is observed by reducing thickness. In such thin films, we also observed a suppression of the MR and weak anti-localization (WAL) effects. We attributed these effects to disorders originated from the extrinsic surface chemical reaction, which is consistent with the density functional theory (DFT) calculations and in-situ STM results. In contrast to samples without encapsulated protection, we discovered an interesting superconducting transition for those samples with hexagonal Boron Nitride (*h*-BN) film protection. Our results indicate that the metallic or superconducting behavior is its intrinsic state, and the insulating behavior is likely caused by surface oxidation in few layer 1T′-$MoTe_2$ flakes.

Keywords two-dimensional materials, metal-insulator transition, layered transition metal dichalcogenides (TMDs), surface oxidation

1 Introduction

Layered transition metal dichalcogenides (TMDs) have attracted considerable attention due to their unusual electronic, structural chemistry properties, and potential application in two-dimensional (2D) devices [1–7]. Recently, the monolayer of 1T′-TMDs MX_2 (e.g., M = W, Mo and X = Te, Se) are proposed as a large gap 2D Topological Insulator (TI) [6, 8], which is also tunable by the application of strain [9] or electronic field [10]. Furthermore, the layered nature of TMD greatly facilitates in nano-fabrication [4], making them an ideal platform to build their heterostructures [11].

Among various TMD materials, 1T′-phase $MoTe_2$ is of particular interest due to its non-trivial characteristics such as non-saturating magneto-resistance (MR) [12–16], unconventional superconductivity in bulk and thin-flakes [12] and the predicted topological phase transition induced by temperature or strain [17, 18]. Unlike bulk system, the thin film of 1T′-$MoTe_2$ exhibits contradictory results, for instance, an insulating behavior owing to bandgap opening [14], or anisotropic Ising superconductivity [19, 20], and so on.

To understand all these different properties, we further investigated 1T′-$MoTe_2$ films with and without protecting *h*-BN flakes. One critical issue for free standing 1T′-$MoTe_2$ films is the chemical instability at the surfaces due to weak Mo-Te bond energy. Amorphous oxide layer is easily formed in ambient environment [21]. It is believed that the electrical transport properties are affected significantly by these surface effects [21–25]. Thus, the understanding of the surface oxidation effect is an essential step for future applications. Although it is highly desired, the direct

control studies have not been rarely performed experimentally. In this work, we carried out a systematic study of the thickness-dependent properties of 1T′-$MoTe_2$ thin films as well as bulk single crystals. For bulk samples, surface effects are negligible and Shubnikov–de Hass(SdH) oscillations are clearly seen at high magnetic fields. However, bare films without protection become insulating when the thickness is tailored below $\sim$ 6 nm. Whereas, signatures of superconductivity are found for films with *h*-BN protection. Our findings suggest that the metallic and superconducting states are intrinsic in $MoTe_2$ films, and that the insulating behavior for bare films is induced by surface degradation. It is further confirmed by the obervation of weak anti-localization effect (WAL), STM measurements, and DFT calculations.

2 Experimental details

Single crystals of 1T′-$MoTe_2$ were synthesized via a flux method with NaCl (see Methods in Ref. [14]). The 1T′-$MoTe_2$ devices without encapsulation are fabricated with the traditional electron beam lithography (EBL) method. We first performed mechanic exfoliation of flakes using scotch tape method from the bulk samples in glove box filled with argon. Then thin flakes of $MoTe_2$ were deposited onto silicon substrate with 300 nm SiO_2 on top and immediately spun polymethyl methacrylate (PMMA) on them. Devices were designed as a conventional Hall-bar configuration via standard EBL with Cr(5 nm)/Au(50 nm) electrodes deposited by thermal evaporation. After lift off, we re-spun PMMA on them to protect these samples. The exposure time was limited to ten minutes in the whole process. As for the devices encapsulated by *h*-BN film, the samples are processed with dry transfer method. Initially, we exfoliated the *h*-BN and 1T′-$MoTe_2$ thin flakes on a thickness of SiO_2 (300 nm)/Si substrates. Next, we used thin *h*-BN film to pick up the $MoTe_2$ flake, and transferred them to the predefined Hall-bar configurations leads [Cr(5 nm)/Au(50 nm)]. Both the mechanic exfoliation and transfer processes are performed in argon gas glove box, which can avoid any exposure to ambient conditions. Magneto-transport measurements of $MoTe_2$ samples were carried out with the four-probe technique with an alternating current of 0.1–1 mA amplitude and a frequency of 10–20 Hz using a Keithley 6221 AC/DC current source. The voltage signal was obtained by a Stanford Research S830 lock-in amplifier. The thickness of the films were measured by the Atomic Force Microscopy after transport measurements.

3 Results and discussion

Figure 1(a) displays the temperature dependence of resistivity for a bulk $MoTe_2$. For our single-crystal $MoTe_2$ sample, we observe that a residual resistivity ratio [RRR = $\rho(300\ \mathrm{K})/\rho(1.5\ \mathrm{K})$] $\sim$ 260 and $\Delta MR = [\rho_{xx}(12\ \mathrm{T}) - \rho_{xx}(0\ \mathrm{T})]/\rho_{xx}(0\ \mathrm{T}) \sim 7.6\times10^3$ % [Fig. 1(b)], both quantities indicate a high-quality crystalline $MoTe_2$. A hysteresis during the warm-up and the cool-down curves caused by the first-order structural transition can be seen around 240 K [13, 14]. The difference of two curves is getting smaller and eventually varnishes below 40 K, which might be due to nearly perfect compensation of electron and hole. In Fig. 1(b), we plot the magnetic field dependence of ρ_{xx} and ρ_{xy} at 1.5 K. The applied current flows along the crystalline *a*-axis and the magnetic field is applied to the *c*-axis. ρ_{xx} shows a nearly quadratic dependence on the magnetic field and no signs of saturation is found up to 13 T. Whereas, ρ_{xy} more or less scales linearly with the magnetic field. SdH oscillations can be found both in ρ_{xx} and ρ_{xy} above 7 T. In Fig. 1(c), the SdH signal extracted from ρ_{xx} is revealed as a function of inverse field of B. In earlier studies, two distinct frequencies at 231 T and 242 T [13, 26] are reported, while only one peak at 251 T is seen by fast Fourier transform in our result within experimental resolution limit [Fig. 1(c) inset]. In Fig. 1(d), we plot the Landau level index n against $1/B$. The Landau level index n is evaluated as the oscillation frequency [see Fig. 1(c) inset] divided by the minima value of magnetic field in ρ_{xx}. The corresponding $1/B$ values are taken from the minima of SdH signal. Linear fitting of the data yields a finite non-zero intercept of 0.5226, which indicates

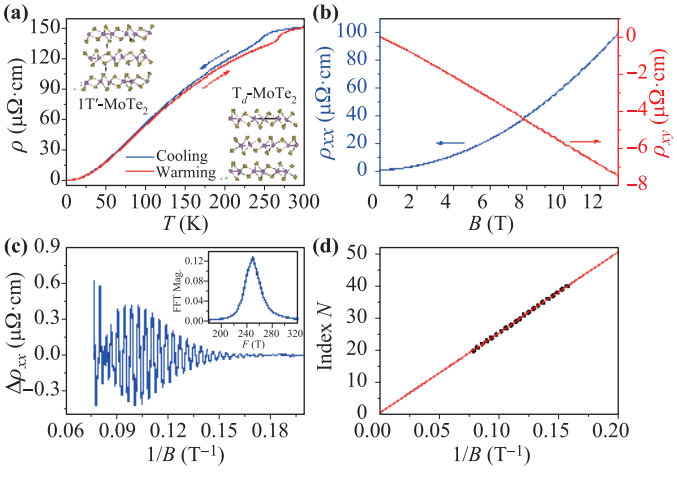

Fig. 1 **(a)** Temperature dependence of resistivity for bulk $MoTe_2$. Red lines and blue line respectively represent temperature sweeping up and down. The atomic structural images denote the monoclinic 1T′ (right-down side) and orthorhombic T_d phase (left-up side), respectively. **(b)** ρ_{xx} (blue line) and ρ_{xy} (red line) for currents flowing along the *a*-axis as a function of a magnetic field at $T = 1.5$ K. **(c)** SdH oscillations as extracted from the ρ_{xx}. Inset: Fast Fourier Transform of the oscillatory signal. **(d)** Landau-level fan diagram for SdH oscillation in $\Delta\rho_{xx}$. Linear fitting of the Landau level index n as a function of periodic minima gives a nonzero intersects around 0.5, corresponding to a nontrivial Berry phase of ϕ.

the existence of non-trivial topological states. All the bulk $MoTe_2$ data is in well agreement with previous results reported in Ref. [13].

Figures 2(a) and (b) show the sheet resistance $R_{sheet}(=\frac{RW}{L})$ as a function of temperature for 1T′-$MoTe_2$ devices with different thicknesses, where R, W and L are the longitudinal resistance, width and length of the devices, respectively. As we reduce the thickness down to 10 nm scale, the first-order structure phase transition occurred in bulk crystals is no longer visible. This implies that thin film form of $MoTe_2$ favors the T_d stacking rather than the intrinsic 1T′ phase at room temperature as reported Ref. [19]. In detail, one can classify these samples into three types based on their different transport properties [Fig. 2(b)]. The first type (11.1 nm to 6.7 nm) carries a metallic characteristic, which is similar to the bulk $MoTe_2$. Then, by further exfoliating $MoTe_2$ down to 4.5 nm, a metal-insulator transition (MIT) appears $\sim$ 20 K for the second type, which is accompanied by a bandgap opening [14]. The bandgap increases gradually as we keep reducing the thickness. Eventually below $\sim$ 4 nm, the samples becomes insulating for the third type. On the contrary, films with h-BN protection remain metallic down to 5.2 nm and even become superconducting below 3 K [see orange line in Fig. 2(a)]. We will discuss the occurrence of superconductivity in detail in a separate work [20]. Figure 2(c) shows a set of typical dI/dV spectra taken at $T = 300$ K. No signature of bandgap is found for pristine sample and to be a metallic system. Once the sample surface is exposed to oxygen within few minutes (3, 6 mins), it degrades rapidly with a bandgap opening up to 100 meV. Figures 2(d) and (e) show the atomically resolved STM topographic images of 1T′-$MoTe_2$ before and after exposure to oxygen. The bright spots showed in Fig. 2(e) imply the surface oxidation of 1T′-$MoTe_2$ after exposure to oxygen. This finding further supports our argument that the insulating transport property of thin $MoTe_2$ flakes is actually attributed to be surface oxidation.

The surface oxide layer developed in TMDs induces disorders that manifest themselves as a 2D impurity band with low mobility, which leads to the suppression of MR for thin flakes [25]. Moreover, disorders are known to cause weak-localization (WL) in graphene [27], and WAL in other systems [28, 29]. Figure 3(a) shows MR defined as $\mathrm{MR} = \frac{R(B)-R(0)}{R(0)}$ for devices with different thicknesses at 1.5 K. Compared with bulk 1T′-$MoTe_2$, MR of these thin films is largely suppressed [refer to Fig. 1(b)], which is caused by disorders induced by surface oxidation. For the samples with the thicknesses of 9.5 nm and 8.1 nm, MR scales as B^2 as at various temperatures [see Fig. 3(d)], which is similar to that of bulk $MoTe_2$. Such an unconventional non-saturating MR behavior can be ascribed to the charge compensation of electron and hole pockets [30]. Meanwhile, for insulating thin films (below $\sim$ 4 nm), clear WAL cusp appears at a low temperatures [Figs. 3(b) and (c)], which arises from disorders by surface contaminations [28, 29].

To further study the effect of surface oxidation in thin $MoTe_2$ flakes, we systematically analyzed the MR of the 4.2 nm and 3.3 nm $MoTe_2$ flakes. WAL can usually be

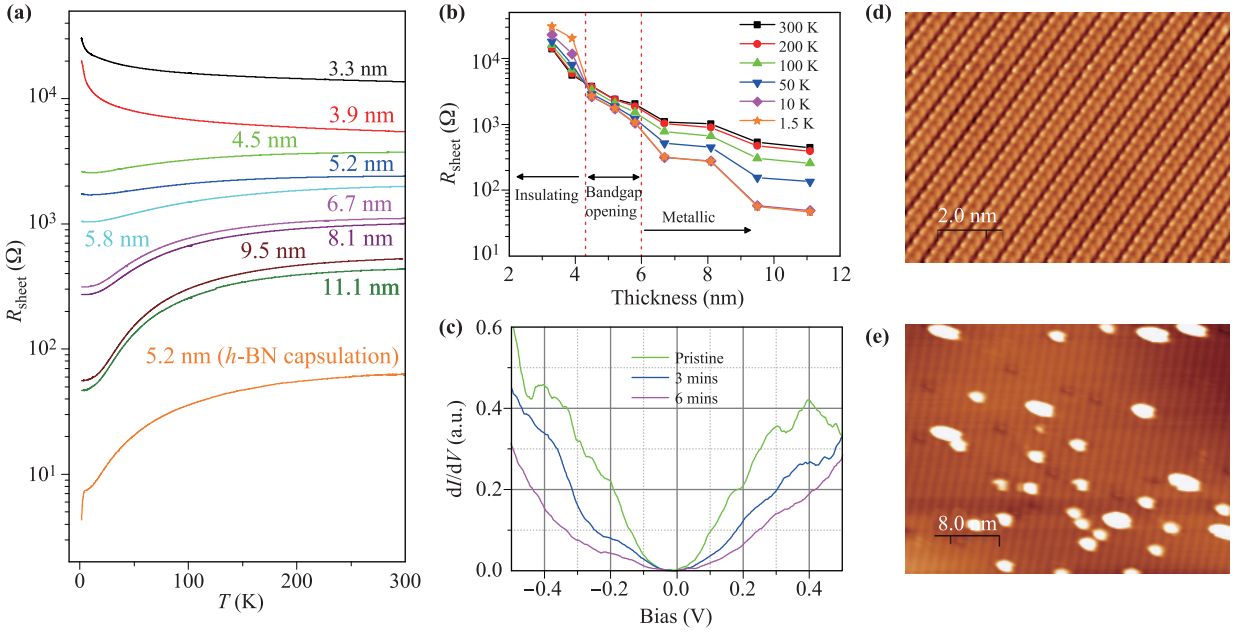

Fig. 2 **(a)** Temperature dependence of sheet resistance $MoTe_2$ films with various thickness. **(b)** Thickness dependence of the sheet resistance for thin films at various temperatures. **(c)** The influence on dI/dV spectrum taken on $MoTe_2$ sample with varied exposure duration to oxygen at room temperature. **(d, e)** Atomically resolved STM topographic images of $MoTe_2$ before and after exposure duration to oxygen several minutes.

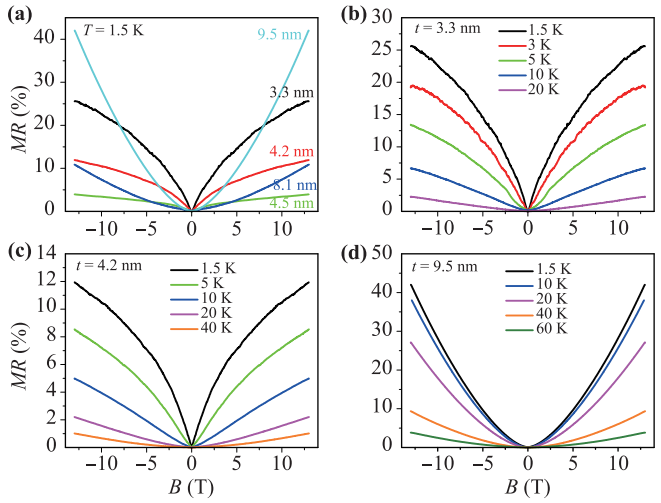

Fig. 3 **(a)** MR data with various thickness (3.3, 4.2, 4.5, 8.1, and 9.5 nm) at 1.5 K. **(b–d)** Each MR result at different temperatures at a certain thicknesses. A clear cusp-like feature can be seen at 3.2 nm $MoTe_2$ thin film device, while it appears a trivial quadratic magnetic field dependence at 9.5 nm.

described by the Hikami–Larkin–Nagaoka (HLM) quantum interference model [31, 32]. In 2D systems, the HLM equation is simplified as

$$\Delta G(B) = -\frac{\alpha e^2}{\pi h}\left[\psi\left(\frac{\hbar}{4eL_\phi^2 B}+\frac{1}{2}\right)-\ln\left(\frac{\hbar}{4eL_\phi^2 B}\right)\right]+\beta B^2, \quad (1)$$

where α is a WAL coefficient associated with the 2D bulk effects, e is the electronic charge, $\hbar$ is the reduced Plank's constant, ψ is the digamma function, L_ϕ is the phase coherence length and β is the quadratic coefficient arising from additional scattering terms (spin–orbit and elastic scattering). The value of α given by the WAL should be -0.5 for perfect 2D case [33–36].

Figures 4(a) and (c) present the magneto-conductance $\Delta G = G(B) - G(0)$ evaluated using data shown in Fig. 3 for 3.3 nm and 4.2 nm devices. The WAL cusps at low temperatures and low-fields region are clearly seen. The WAL cusps fade away at higher temperature as the phase coherence length becomes shorter and a quadratic B-dependence is recovered eventually.

In fact, our data can be well described by the modified HLN equation [Eq. (1)] as shown in red solid lines in Figs. 4(a) and (c). The fitting results of α and L_ϕ of 4.2 nm and 3.3 nm samples are shown in Figs. 4(c) and (d). The obtained L_ϕ points fall onto a power-law scaling $L_\phi \propto T^{-0.5}$ [red curves in Figs. 4(c) and (d)] for both devices over wide temperature range, which confirms the 2D nature of WAL in our system. The coefficient α takes a value of $\alpha = 1/2$ for a traditional 2D electron system with strong spin-orbit coupling and one helical surface with a single Dirac cone. For 4.2 nm sample, α takes a value of -0.8 at 1.5 K. It grows in magnitude upon warming. This may be interpreted as a coherent impurity-to-bulk scattering channel switching. Below 10 K, the impurity-to-bulk scattering length is smaller than coherence length whereas it becomes larger than coherence length above 10 K [37]. As for the 3.3 nm device with a larger bandgap, the fitting parameters α is apparently smaller than that of 4.2 nm sample [Fig. 4(d) blue dots]. This implies that the number of channels is also reduced in thinner samples. Compared to 4.2 nm device, increment of α extends to higher temperature 15 K. It is guaranteed by larger phase coherence length and smaller impurity-to-bulk scattering length in thinner samples. Hence, our analysis suggests that the WAL effects observed in thin $MoTe_2$ flakes is caused by localization effects induced by surface disorders.

In order to verify that the surface oxidation can induce bandgap opening in monolayer 1T′-$MoTe_2$, we calculated the band structures of both pristine 1T′-$MoTe_2$ (Model_1) and the surface oxided systems (Model_2, Model_3, Model_4). We performed first-principles calculations based on the density functional theory (DFT) using the projector augmented wave method as implemented in the Vienna c simulation package [38–40]. The exchange-correlation functional was modeled within the generalized gradient approximation (GGA) with the Perdew–Burke–Ernzerhof (PBE) realization [41]. The cutoff energy was chosen as 550 eV, and the Brillouin zone (BZ) was sampled with a Γ-centered k mesh of size $8 \times 14 \times 1$. The energy and force convergence criteria were set to be 10^{-5} eV and 0.01 eV, respectively. The lattice parameters shown in Table 1 were fully optimized until all the forces and stress tensor were minimized. As for the calculation of band structures, hybrid functional (HSE06) was used as

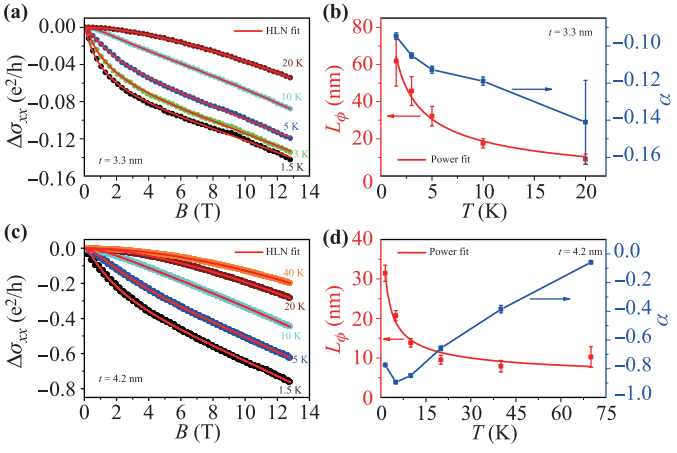

Fig. 4 Temperature-dependent magnetoresistance of the 4.2 nm and 3.3 nm thick nanoflake $MoTe_2$. **(a, c)** Magnetoconductance versus applied magnetic field for 4.2 nm and 3.3 nm $MoTe_2$ at various temperatures. The HNL fitting curves are plotted in black solid lines. **(b, d)** The parameters got from HLN model fitting versus temperatures for 4.3 nm and 3.3 nm $MoTe_2$. The power-law fit (red solid lines) gives $L_\phi \propto T^{-0.5}$ in the temperature regime 1.5 to 70 K **(b)** and 1.5 to 20 K **(d)**, respectively.

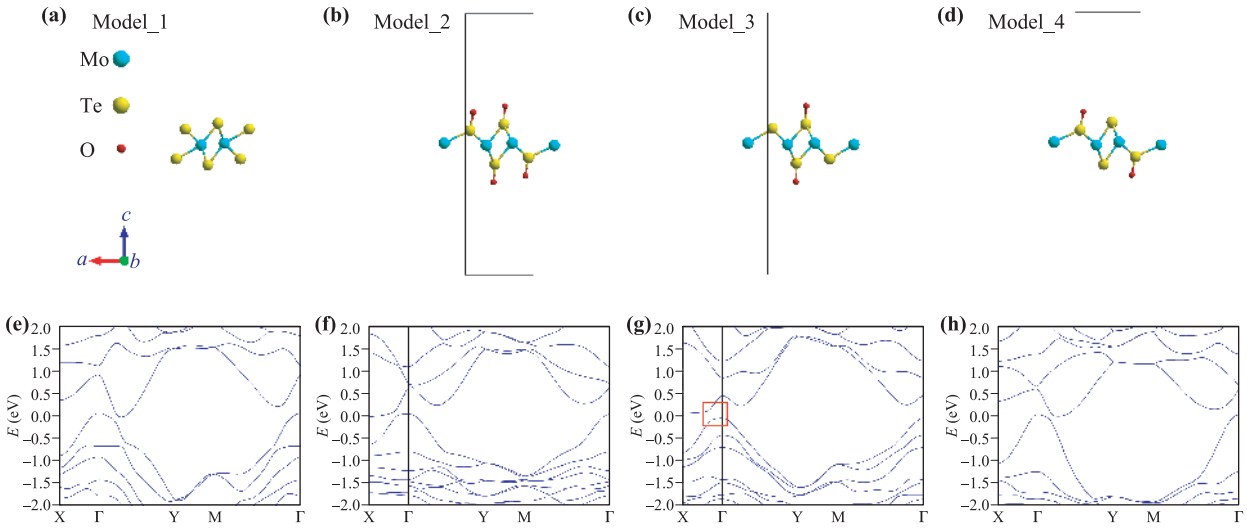

Fig. 5 **(a–d)** Schematic diagrams of pristine 1T′-$MoTe_2$ (Model_1) and its surface oxided systems (Model_2, Model_3, Model_4) in ball-stick presentations. **(e–h)** Band structures of 1T′-$MoTe_2$ systems with (Model_2, Model_3, Model_4) and without (Model_1) surface oxidation.

Table 1 The optimized lattice parameters of 1T′-$MoTe_2$ and its surface oxided systems.

	Model_1	Model_2	Model_3	Model_4	Experiment result
a (Å)	6.355	6.714	6.558	6.442	6.57
b (Å)	3.469	3.533	3.488	3.522	3.47

the exchange-correlation potential [42]. For the pristine 1T′-$MoTe_2$ (Mode 1), the calculated band structure shows a local gap along the path Γ–Y, which remains a metallic behavior. Surface chemical instabilities in $MoTe_2$ drive the development of amorphous surface oxide (Model_2, Model_3, Mode_4) in ambient conditions. Among the three models, the optimized lattice constant of Model_3 is closest to the experimental results measured at 4.8 K. The band structure of Model_3 shows a bandgap opening along the path Γ-X with a gap value of 104 meV [marked with a red box in Fig. 5(g)], which is in agreement with the STM observations. Therefore, the bandgap opening observed in thin films of 1T′-$MoTe_2$ is likely to result from the surface oxidation.

4 Conclusion

In conclusion, combining transport, STM measurements, and theoretical calculations, we have studied in detail the thickness-dependent properties of 1T′-$MoTe_2$ from bulk to few layers. In bulk samples, we confirmed a non-trivial phase shift in quantum oscillation, which is consistent with the non-trivial topological states. In thin flake samples without encapsulation, an insulating behavior is observed when the thickness is tailored below ∼ 6 nm. In contrast, we find that the thin flakes of 1T′-$MoTe_2$ fully encapsulated in h-BN stay metallic and even become superconducting below 3 K. In addition, the in-situ STM measurements and band structrue calculation also provide strong evidence of insulating states from surface oxidation. Our results suggest that the intrinsic electronic properties in thin $MoTe_2$ flakes is likely a superconducting state, and that the insulating behavior originated from surface oxidation, rather than a bandgap opening from spin–orbit coupling (SOC) due to reduced dimensions [14].

Acknowledgements The work was supported by the Guangdong Innovative and Entrepreneurial Research Team Program, China (Grant No. 2016ZT06D348), the National Natural Science Foundation of China (Grant No. 11874193), and the Shenzhen Fundamental Subject Research Program, China (Grant No. JCYJ20170817110751776). K. D. W. acknowledges support from the National Natural Science Foundation of China (Grant No. 11574128). X. D. acknowledges support from NSF under award DMR-1808491.

References

1. J. A. Wilson and A. D. Yoffe, The transition metal dichalcogenides discussion and interpretation of the observed optical, electrical and structural properties, *Adv. Phys.* 18(73), 193 (1969)
2. R. C. Morris, R. V. Coleman, and R. Bhandari, Superconductivity and magnetoresistance in $NbSe_2$, *Phys. Rev. B* 5(3), 895 (1972)
3. M. Chhowalla, H. S. Shin, G. Eda, L. J. Li, K. P. Loh,

and H. Zhang, The chemistry of two-dimensional layered transition metal dichalcogenide nanosheets, *Nat. Chem.* 5(4), 263 (2013)

4. B. Radisavljevic, A. Radenovic, J. Brivio, V. Giacometti, and A. Kis, Single-layer MoS_2 transistors, *Nat. Nanotechnol.* 6(3), 147 (2011)
5. R. A. Klemm, Pristine and intercalated transition metal dichalcogenide superconductors, *Physica C* 514, 86 (2015)
6. X. Qian, J. Liu, L. Fu, and J. Li, Quantum spin Hall effect in two-dimensional transition metal dichalcogenides, *Science* 346(6215), 1344 (2014)
7. K. Novoselov, D. V. Andreeva, W. Ren, and G. Shan, Graphene and other two-dimensional materials, *Front. Phys.* 14(1), 13301 (2019)
8. J. Qi, H. Liu, H. Jiang, and X. C. Xie, Dephasing effects in topological insulators, *Front. Phys.* 14(4), 43403 (2019)
9. T. Teshome and A. Datta, Topological insulator in two-dimensional SiGe induced by biaxial tensile strain, *ACS Omega* 3(1), 1 (2018)
10. Q. Liu, X. Zhang, L. B. Abdalla, A. Fazzio, and A. Zunger, Switching a normal insulator into a topological insulator via electronic field with application to phosphorene, *Nano Lett.* 15(2), 1222 (2015)
11. A. K. Geim and I. V. Grigorieva, Van der Waals heterostructures, *Nature* 499(7459), 419 (2013)
12. Y. Qi, P. G. Naumov, M. N. Ali, C. R. Rajamathi, W. Schnelle, O. Barkalov, M. Hanfland, S. C. Wu, C. Shekhar, Y. Sun, V. Süß, M. Schmidt, U. Schwarz, E. Pippel, P. Werner, R. Hillebrand, T. Förster, E. Kampert, S. Parkin, R. J. Cava, C. Felser, B. Yan, and S. A. Medvedev, Superconductivity in Weyl semimetal candidate $MoTe_2$, *Nat. Commun.* 7(1), 11038 (2016)
13. Q. Zhou, D. Rhodes, Q. R. Zhang, S. Tang, R. Schönemann, and L. Balicas, Hall effect within the colossal magnetoresistive semimetallic state of $MoTe_2$, *Phys. Rev. B* 94(12), 121101 (2016)
14. D. H. Keum, S. Cho, J. H. Kim, D. H. Choe, H. J. Sung, M. Kan, H. Kang, J. Y. Hwang, S. W. Kim, H. Yang, K. J. Chang, and Y. H. Lee, Bandgap opening in fewlayered monoclinic $MoTe_2$, *Nat. Phys.* 11(6), 482 (2015)
15. H. P. Hughes and R. H. Friend, Electrical resistivity anomaly in *b*-$MoTe_2$ (metallic behavior), *J. Phys. C Solid State Phys.* 11(3), L103 (1978)
16. T. Zandt, H. Dwelk, C. Janowitz, and R. Manzke, Quadratic temperature dependence up to 50 K of the resistivity of metallic $MoTe_2$, *J. Alloys Compd.* 442(1–2), 216 (2007)
17. Y. Sun, S. C. Wu, M. N. Ali, C. Felser, and B. Yan, Prediction of Weyl semimetal in orthorhombic $MoTe_2$, *Phys. Rev. B* 92(16), 161107 (2015)
18. R. Szczśniak, A. P. Durajski, and M. W. Jarosik, Strong-coupling superconductivity induced by calcium intercalation in bilayer transition-metal dichalcogenides, *Front. Phys.* 13(2), 137401 (2018)
19. J. Cui, P. Li, J. Zhou, W. Y. He, X. Huang, J. Yi, J. Fan, Z. Ji, X. Jing, F. Qu, Z. G. Cheng, C. Yang, L. Lu, K. Suenaga, J. Liu, K. T. Law, J. Lin, Z. Liu, and G. Liu, Transport evidence of asymmetric spin-orbit coupling in few-layer superconducting 1T*d*-$MoTe_2$, *Nat. Commun.* 10(1), 2044 (2019)
20. Y. Gan, C.W. Cho, A. Li, J. Lyu, X. Du, J. S. Wen, and L. Y. Zhang, Giant enhancement of superconductivity in few layers $MoTe_2$, *Chin. Phys. B* 28(11), 117401 (2019)
21. L. Yang, H. Wu, W. Zhang, Z. Chen, J. Li, X. Lou, Z. Xie, R. Zhu, and H. Chang, Anomalous oxidation and its effect on electrical transport originating from surface chemical instability in large-area, few-layer 1T′-$MoTe_2$ films, *Nanoscale* 10(42), 19906 (2018)
22. F. Ye, J. Lee, J. Hu, Z. Mao, J. Wei, and P. X. L. Feng, Environmental instability and degradation of singleand few-layer WTe_2 nanosheets in ambient conditions, *Small* 12(42), 5802 (2016)
23. B. Chen, H. Sahin, A. Suslu, L. Ding, M. I. Bertoni, F. M. Peeters, and S. Tongay, Environmental changes in $MoTe_2$ excitonic dynamics by defects-activated molecular interaction, *ACS Nano* 9(5), 5326 (2015)
24. H. Zhu, Q. Wang, L. Cheng, R. Addou, J. Kim, M. J. Kim, and R. M. Wallace, Defects and surface structural stability of $MoTe_2$ under vacuum annealing, *ACS Nano* 11(11), 11005 (2017)
25. J. M. Woods, J. Shen, P. Kumaravadivel, Y. Pang, Y. Xie, G. A. Pan, M. Li, E. I. Altman, L. Lu, and J. J. Cha, Suppression of magnetoresistance in thin WTe_2 flakes by surface oxidation, *ACS Appl. Mater. Interfaces* 9(27), 23175 (2017)
26. D. Rhodes, R. Schönemann, N. Aryal, Q. Zhou, Q. R. Zhang, E. Kampert, Y.C. Chiu, Y. Lai, Y. Shimura, G. T. McCandless, J. Y. Chan, D. W. Paley, J. Lee, A. D. Finke, J. P. C. Ruff, S. Das, E. Manousakis, and L. Balicas, Bulk Fermi surface of the Weyl type-II semimetallic candidate *g*-$MoTe_2$, *Phys. Rev. B* 96(16), 165134 (2017)
27. I. Childres, L. A. Jauregui, J. Tian, and Y. P. Chen, Effect of oxygen plasma etching on graphene studied using Raman spectroscopy and electronic transport measurements, *New J. Phys.* 13(2), 025008 (2011)
28. B. Zhao, P. Cheng, H. Pan, S. Zhang, B. Wang, G. Wang, F. Xiu, and F. Song, Weak antilocalization in Cd_3As_2 thin films, *Sci. Rep.* 6(1), 22377 (2016)
29. N. P. Breznay, H. Volker, A. Palevski, R. Mazzarello, A. Kapitulnik, and M. Wuttig, Weak antilocalization and disorder-enhanced electron interactions in annealed films of the phase-change compound $GeSb_2Te_4$, *Phys. Rev. B* 86(20), 205302 (2012)
30. Y. Wu, N. H. Jo, M. Ochi, L. Huang, D. Mou, S. L. Bud'ko, P. C. Canfield, N. Trivedi, R. Arita, and A. Kaminski, Temperature-induced Lifshitz transition in WTe_2, *Phys. Rev. Lett.* 115(16), 166602 (2015)
31. S. Hikami, A. I. Larkin, and Y. Nagaoka, Spin–orbit interaction and magnetoresistance in the two dimensional random system, *Prog. Theor. Phys.* 63(2), 707 (1980)

32. G. Bergmann, Weak localization in thin films: A time-offlight experiment with conduction electrons, *Phys. Rep.* 107(1), 1 (1984)
33. J. Chen, H. J. Qin, F. Yang, J. Liu, T. Guan, F. M. Qu, G. H. Zhang, J. R. Shi, X. C. Xie, C. L. Yang, K. H. Wu, Y. Q. Li, and L. Lu, Gate-voltage control of chemical potential and weak antilocalization in Bi_2Se_3, *Phys. Rev. Lett.* 105(17), 176602 (2010)
34. H. T. He, G. Wang, T. Zhang, I. K. Sou, G. K. L. Wong, J. N. Wang, H. Z. Lu, S. Q. Shen, and F. C. Zhang, Impurity effect on weak antilocalization in the topological insulator Bi_2Te_3, *Phys. Rev. Lett.* 106(16), 166805 (2011)
35. J. J. Cha, D. Kong, S. S. Hong, J. G. Analytis, K. Lai, and Y. Cui, Weak antilocalization in $Bi_2(Se_xTe_{1-x})_3$ nanoribbons and nanoplates, *Nano Lett.* 12(2), 1107 (2012)
36. S. Matsuo, T. Koyama, K. Shimamura, T. Arakawa, Y. Nishihara, D. Chiba, K. Kobayashi, T. Ono, C. Z. Chang, K. He, X. C. Ma, and Q. K. Xue, Weak antilocalization and conductance fluctuation in a submicrometer-sized wire of epitaxial Bi_2Se_3, *Phys. Rev. B* 85(7), 075440 (2012)
37. H. Steinberg, J. B. Laloë, V. Fatemi, J. S. Moodera, and P. Jarillo-Herrero, Electrical tunable surface-to-bulk coherent coupling in topological insulator thin films, *Phys. Rev. B* 84(23), 233101 (2011)
38. G. Kresse and J. Hafner, *ab initio* molecular-dynamics simulation of the liquid-metal-amorphous-semiconductor transition in germanium, *Phys. Rev. B* 49(20), 14251 (1994)
39. G. Kresse and J. Furthmüller, Efficient iterative schemes for *ab initio* total-energy calculations using a plane-wave basis set, *Phys. Rev. B* 54(16), 11169 (1996)
40. P. E. Blöchl, Projector augmented-wave method, *Phys. Rev. B* 50(24), 17953 (1994)
41. J. P. Perdew, K. Burke, and M. Ernzerhof, Generalized gradient approximation made simple, *Phys. Rev. Lett.* 77(18), 3865 (1996)
42. J. Heyd, G. E. Scuseria, and M. Ernzerhof, Hybrid functionals based on a screened coulomb potential, *J. Chem. Phys.* 118(18), 8207 (2003)